Extreme Mechanics Letters 64 (2023) 102082

Contents lists available at ScienceDirect

Extreme Mechanics Letters

journal homepage: www.elsevier.com/locate/eml

Geometry-informed dynamic mode decomposition in Kresling origami dynamics

Shuaifeng Li [a], Yasuhiro Miyazawa [a], Koshiro Yamaguchi [a], Panayotis G. Kevrekidis [b], Jinkyu Yang [a,c,*]

[a] Department of Aeronautics and Astronautics, University of Washington, Seattle, 98195, WA, USA
[b] Department of Mathematics and Statistics, University of Massachusetts, Amherst, 01003, MA, USA
[c] Department of Mechanical Engineering, Seoul National University, Seoul, 08826, Republic of Korea

ARTICLE INFO

Keywords:
Dynamic mode decomposition
Origami
Origami dynamics

ABSTRACT

Origami structures often serve as the building block of mechanical systems due to their rich static and dynamic behaviors. Experimental observation and theoretical modeling of origami dynamics have been reported extensively, whereas the data-driven modeling of origami dynamics is still challenging due to the intrinsic nonlinearity of the system. In this study, we show how the dynamic mode decomposition (DMD) method can be enhanced by integrating geometry information of the origami structure to model Kresling origami dynamics in an efficient and accurate manner. In particular, an improved version of DMD with control, that we term geometry-informed dynamic mode decomposition (giDMD), is developed and evaluated on the origami chain and dual Kresling origami structure to reveal the efficacy and interpretability. We show that giDMD can accurately predict the dynamics of an origami chain across frequencies, where the topological boundary state can be identified by the characteristics of giDMD. Moreover, the periodic intrawell motion can be accurately predicted in the dual origami structure. The type of dynamics in the dual origami structure can also be identified. The model learned by the giDMD also reveals the influential geometrical parameters in the origami dynamics, indicating the interpretability of this method. The accurate prediction of chaotic dynamics remains a challenge for the method. Nevertheless, we expect that the proposed giDMD approach will be helpful towards the prediction and identification of dynamics in complex origami structures, while paving the way to the application to a wider variety of lightweight and deployable structures.

1. Introduction

Origami, as an ancient handcrafted paper folding art, captivates not only artists and mathematicians with its exquisite design principles, but also engineers with its enormous (and increasingly leveraged in recent years) potential in engineering applications. By introducing the principles of creasing and folding to the flat materials, origami structures can be formed, which lead to stiffness enhancement [1], negative Poisson's ratio [2,3] and multistability in the architecture [4–6]. These developments also inspire further applications in the robotics [7,8], medical equipment [9,10], and mechanical metamaterials with unprecedented mechanical properties [11,12]. Aside from the aforementioned static and quasi-static mechanical properties, origami also possesses rich dynamics that can be used to construct prospective engineering devices for impact mitigation and vibration control, which has been studied using experiments, numerical simulations, and modeling [13–17].

In recent years, the modeling and analysis of dynamical systems via data-driven approaches have grown in popularity because they require little expert knowledge of the governing equations [18–20]. Specifically, origami nonlinear dynamics have been realized with excellent accuracy by machine learning methods based on neural networks [16]. However, machine learning based on the neural networks is typically computationally intensive and time-consuming at the training stage. Furthermore, the model works as a gigantic black box where the decision processes are difficult to understand and cannot explicitly reveal the underlying physics behind the origami dynamics, despite the fact that a recent study based on the recurrent neural network can mimic the Lyapunov exponent of chaotic origami motions from the hidden layer [16].

In light of this, some novel data-driven frameworks to discover underlying dynamics and physics have been developed such as sparse identification of nonlinear dynamics (SINDy) [21] and dynamic mode decomposition (DMD) [22]. Therein, DMD, as one of the most effective machine learning techniques, has recently been used in many

* Corresponding author at: Department of Mechanical Engineering, Seoul National University, Seoul, 08826, Republic of Korea.
E-mail address: jkyang11@snu.ac.kr (J. Yang).

https://doi.org/10.1016/j.eml.2023.102082
Received 17 July 2023; Received in revised form 30 August 2023; Accepted 19 September 2023
Available online 22 September 2023

fields for its simplicity and interpretability. Given the advantages of DMD and relation between DMD and Koopman mode decomposition, DMD is suitable for characterizing various nonlinear physical and biological systems [23]. Originally, DMD was developed to identify spatiotemporal coherent structures from high-dimensional data in the fluid dynamics community [24]. In addition to fluid dynamics, DMD has been successfully applied to the analysis of biological signals and structural dynamics [25–27], as well as more recently to topological metamaterials [28]. In these studies, DMD features fast computation and excellent interpretability by a series of physically coherent structures. However, for the systems with control, DMD is not capable of uncovering the role that the control plays in the system. In light of this, DMD with control (DMDc), a variant of DMD, is proposed to relate the state and the control of a system, highlighting the importance of the control and improving the accuracy of the DMD model [29,30]. On the other hand, DMDc often ends up with low accuracy or failure to model several nonlinear systems [31]. Therefore, it would be worthwhile to investigate an improved version of DMD for origami dynamics given the needs of data-driven modeling in this field and inherent deficiencies in the current DMD formulations.

In our work, we introduce a data-driven framework called geometry-informed dynamic mode decomposition (giDMD), which is capable of capturing spatiotemporal dynamics of the Kresling origami structures under excitation. By integrating the geometry information of origami into the DMDc, it becomes possible to not only demonstrate the high accuracy of our approach compared with the DMDc, but also reveal the role of the geometrical parameters in the dynamics, showcasing the interpretability. This approach can also be applied to more complicated Kresling origami structures: origami chain and dual origami structure. In the origami chain, the dynamics across frequencies can be predicted precisely and the frequency of the topological boundary state is identified from the features of giDMD. In the dual origami structure under the excitation in different frequencies, the intrawell periodic motion is predicted accurately. The interwell periodic motion and chaotic dynamics can be identified from the characteristics of giDMD, yet the latter also poses some limitations (regarding the accuracy of its temporal representation) which are of relevance to consider in future studies. Our approach, which is considerably easier to operate and more interpretable than the machine learning based on the neural networks, offers a general technique to handle the origami dynamics in the presence of geometrical parameters.

2. Methods

Fig. 1(a) illustrates the side and top views of the single Kresling origami structure. This single origami structure has two coupled degrees of freedom on the separator: translational motion along the vertical direction u and rotational motion around vertical direction ϕ, resulting in the rotation of the top surface following the compression of the origami [14]. This coupled behavior is described by a truss model which is composed of the lumped masses and discs connected by the springs. Appendix A shows the governing equations of motion for the origami coupled features. The creasing and folding of the origami structure also introduce numerous geometrical variables which are marked in Fig. 1. h, a, b, α, β, and Ψ represent the height, the length of crease lines, the angles between the crease lines and the vertical direction, and folding angle (the angle between the horizontal plane and facet). During the compression and tension of the origami structure, according to the geometric constraints, these geometrical variables will change as a function of axial and rotational displacement as shown below:

$$h = h_0 - \delta u \tag{1}$$

$$a = \sqrt{(h_0 - \delta u)^2 + 4R^2 \sin^2(\frac{\delta\phi}{2} + \frac{\theta_0}{2} - \frac{\pi}{2N})} \tag{2}$$

$$b = \sqrt{(h_0 - \delta u)^2 + 4R^2 \sin^2(\frac{\delta\phi}{2} + \frac{\theta_0}{2} + \frac{\pi}{2N})} \tag{3}$$

$$\Psi = \arctan \frac{h_0 - \delta u}{R[\cos(\frac{\pi}{N}) - \cos(\delta\phi + \theta_0)]} \tag{4}$$

where the δu and $\delta\phi$ represent the differences of axial and rotational displacements between top and bottom surfaces, respectively. h_0, θ_0, R, and N are initial height, initial rotation angle representing the chirality, radius, and number of vertices of the polygonal cross-section. Accordingly, the angles between the crease lines and the vertical direction can be easily calculated. Under the excitation, axial and rotational displacement will vary over time, hence leading to the variation of geometrical parameters. In Fig. 1(b), the vector of geometrical parameters for nth origami element at time t is shown as g_t^n containing h_t^n, a_t^n, b_t^n, Ψ_t^n, α_t^n and β_t^n. Note that the geometrical variables are not limited to the aforementioned six parameters, but can be extended to further geometrical variables potentially present within the origami structures. For better interpretability on how geometrical variables contribute to the origami dynamics, the variants of geometrical variables, such as the square root and squares of them, are not considered.

DMDc is a data-driven approach to model the systems under control, which includes the scenario that the origami structure is excited by an input (the control). DMDc uses a state transition matrix $\boldsymbol{A}$ and the control matrix $\boldsymbol{B}$ to relate the system displacement d_t and the control d_t^c according to:

$$d_{t+1} = \boldsymbol{A} d_t + \boldsymbol{B} d_t^c \tag{5}$$

Depending on whether $\boldsymbol{B}$ is known or not, DMDc has different procedures to obtain the model [29]. Herein, we propose a variant that we term geometry-informed DMD based on DMDc. In particular, we refer to geometry-informed DMD (giDMD) as the DMDc learning framework that integrates underlying knowledge of the origami geometrical variables g_t^n. More concretely, in our present origami setting, we create an augmented state of the nth origami x_t^n composed of the displacement d_t^n and velocity v_t^n in both axial and rotational directions, resulting in $x_t \in \mathbb{R}^{4n}$. An augmented control y_t^n is also created by concatenating the augmented state of the control and the vector of geometrical parameters, resulting in $y_t \in \mathbb{R}^l$, where l is the number of control variables. The vector of geometrical parameters also includes the trigonometric functions (sine and cosine functions) of quantities related to angles, but for simplicity of depicting our approach in a general way, we do not illustrate them in Fig. 1(b). A similar idea using the augmented state and control variables can also be found in the modeling of swarm dynamics [30]. Therefore, the system can be modeled in the form:

$$x_{t+1} = x_t + \boldsymbol{K} y_t \tag{6}$$

where $\boldsymbol{K} \in \mathbb{R}^{4n\times l}$. In giDMD, motivated from the earlier work of [30], the state transition matrix $\boldsymbol{A}$ is assumed to be identity ($\boldsymbol{A} = \boldsymbol{I}$) because we assume that the difference between x_{t+1} and x_t ascribes to the contribution of the control. The Eq. (6) can be rewritten as:

$$x_{t+1} - x_t = \boldsymbol{K} y_t \tag{7}$$

Furthermore, Eq. (7) can be written in the matrix form:

$$\boldsymbol{X}' - \boldsymbol{X} = \boldsymbol{K}\boldsymbol{Y} \tag{8}$$

$$\boldsymbol{S} = \boldsymbol{K}\boldsymbol{Y} \tag{9}$$

where $\boldsymbol{X}' \in \mathbb{R}^{4n\times(T-1)}$ is one snapshot forward compared with $\boldsymbol{X} \in \mathbb{R}^{4n\times(T-1)}$, $\boldsymbol{S} = \boldsymbol{X}' - \boldsymbol{X}$ and $\boldsymbol{Y} \in \mathbb{R}^{l\times(T-1)}$ contains m control variables and $(T-1)$ snapshots. T is the total number of snapshots. Therefore, the matrix $\boldsymbol{K}$ is the key for giDMD modeling, which can be solved by the optimization problem:

$$\arg\min_{\boldsymbol{K}} \left[\frac{1}{2}\|\boldsymbol{S} - \boldsymbol{K}\boldsymbol{Y}\|^2 + \eta R(\boldsymbol{K})\right] \tag{10}$$

where $R(\cdot)$ is a regularizer that promotes sparsity and η is a hyperparameter to determine the strength of the regularization. A sparse

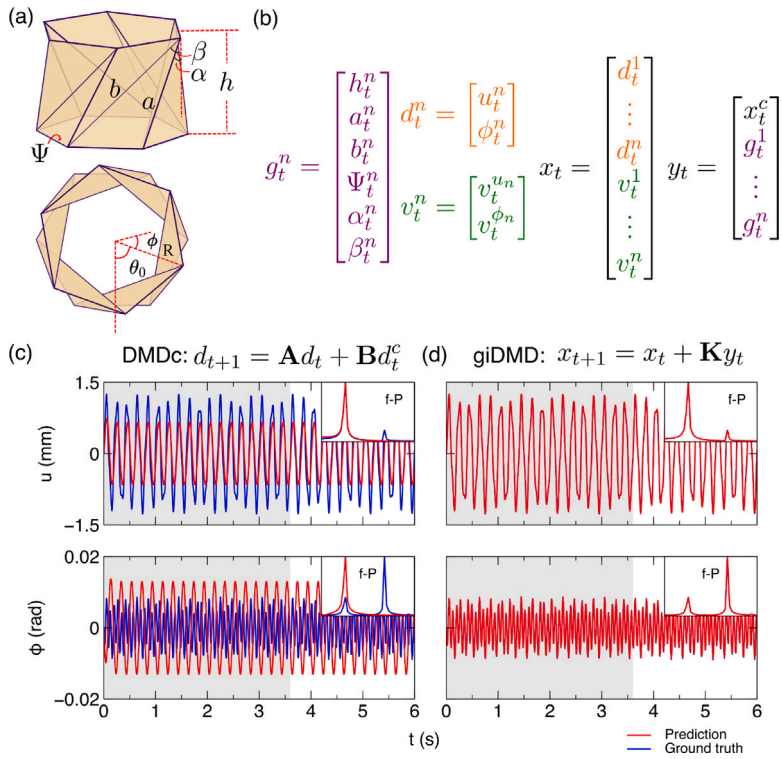

Fig. 1. Illustration of giDMD and comparison between DMDc and giDMD. (a) The side view and the top view of the single Kresling origami with geometrical parameters. (b) The data matrices for the data-driven framework of giDMD. The geometrical parameters g are collected as the height h, the length of crease lines a, b, folding angle Ψ, the direction of the crease lines α, β. The state x is taken to include the displacement p and velocity v, and the control y is taken to involve the states of the input x^c and the geometrical parameters g. (c) The prediction using DMDc. (d) The prediction using giDMD. The predictions of axial displacement u and rotational displacement ϕ using DMDc are shown in the first and second row, respectively. The gray shaded areas represent the training data. The ground truth and the prediction are shown in blue and red, respectively. The insets in four graphs show the relation between frequency (f) and power amplitude (P) after the fast Fourier transform. (For interpretation of the references to color in this figure legend, the reader is referred to the web version of this article.)

matrix $\boldsymbol{K}$ can be useful to promote the interpretation of the role geometries play in the origami dynamics and to discover the dominant geometric components. We use the non-convex regularizer, l_0 norm, in our optimization problem, where sequential thresholded least squares method is performed, which is also widely used in the dynamics discovery [21]. l_0 regularization works by encouraging the coefficients of the model below a certain threshold value to be completely ignored and has convergence guarantees [32]. To be specific, first of all, the standard least squares fitting is performed. Then, a parameter η is given to specify the minimum magnitude for coefficients in $\boldsymbol{K}$ and all coefficients with magnitude below the threshold are zeroed out. This process of fitting and thresholding is performed until convergence. In this way, a sparse matrix $\boldsymbol{K}$ that balances the tradeoff between accuracy and minimizing the number of the control elements can be obtained. In our examples demonstrated below, the rapid convergence is realized within several iterating steps (at most 1 step for single origami, 2 steps for dual origami structures, and 10 steps for origami chain).

Indeed, our method, from the idea of dynamics discovery using sparse regression, is quite similar to SINDy [21]. The sparse $\boldsymbol{K}$ in giDMD and the sparse $\boldsymbol{\Xi}$ in SINDy both serve to select the active terms in the library (control variables in giDMD and candidate functions in SINDy). However, there are some differences. In SINDy, there exists an extensive library of candidate functions that is provided as a possible basis to represent the dynamics, while $\boldsymbol{Y}$ in giDMD only contains the origami geometrical variables. Moreover, the exact velocity and acceleration of the system are used in the SINDy, while $\boldsymbol{S}$ in giDMD, motivated by the DMDc approach, is composed of the difference of displacement and the difference of velocity.

Next, we demonstrate the superiority of our method over the standard DMDc. We simulate the dynamics of a single origami element under the harmonic excitation at the frequency of 5 Hz using the truss model, as detailed in Appendix A. Due to the coupled behavior of the origami features, the output is the axial displacement u and rotational displacement ϕ. When the origami dynamics is modeled by DMDc using 60% training data, both predicted displacements $\hat{u}$ and $\hat{\phi}$ exhibit large discrepancies compared with the simulated displacements u and ϕ in Fig. 1(c). The relative errors calculated by $\frac{\|u-\hat{u}\|_F}{\|u\|_F}$ and $\frac{\|\phi-\hat{\phi}\|_F}{\|\phi\|_F}$ are around 50% and 247% for u and ϕ, where $\|\cdot\|_F$ is the Frobenius norm of the matrix, defined as the square root of the sum of the absolute squares of the entries. In comparison, the significant improvement is achieved by giDMD model, as shown by the agreement between prediction (red lines) and ground truth (blue lines) in Fig. 1(d). The relative errors for u and ϕ are around 0.26% and 1.37%. This improvement can also be seen in the spectra (insets in Figs. 1(c) and 1(d)) given by the fast Fourier transform. Under the excitation of 5 Hz, there is another peak other than the excitation frequency in the spectrum because of the nonlinearity. In stark contrast with the DMDc, giDMD can predict two peaks in the spectrum, implying that giDMD can fully capture the origami dynamics. The drastic improvement in accuracy in both time and frequency domain demonstrates the effectiveness of giDMD towards modeling origami dynamics.

3. Results and discussions

3.1. Topological boundary states in the origami chain

The effectiveness of our method has emerged in the single origami structure above. Next, we further demonstrate this method on more complex origami structures. The first example we demonstrate our method on is the elastic topological metamaterials built by the origami structure. The elastic topological metamaterials are inspired by the electronic topological insulators, where the vibration is isolated in the

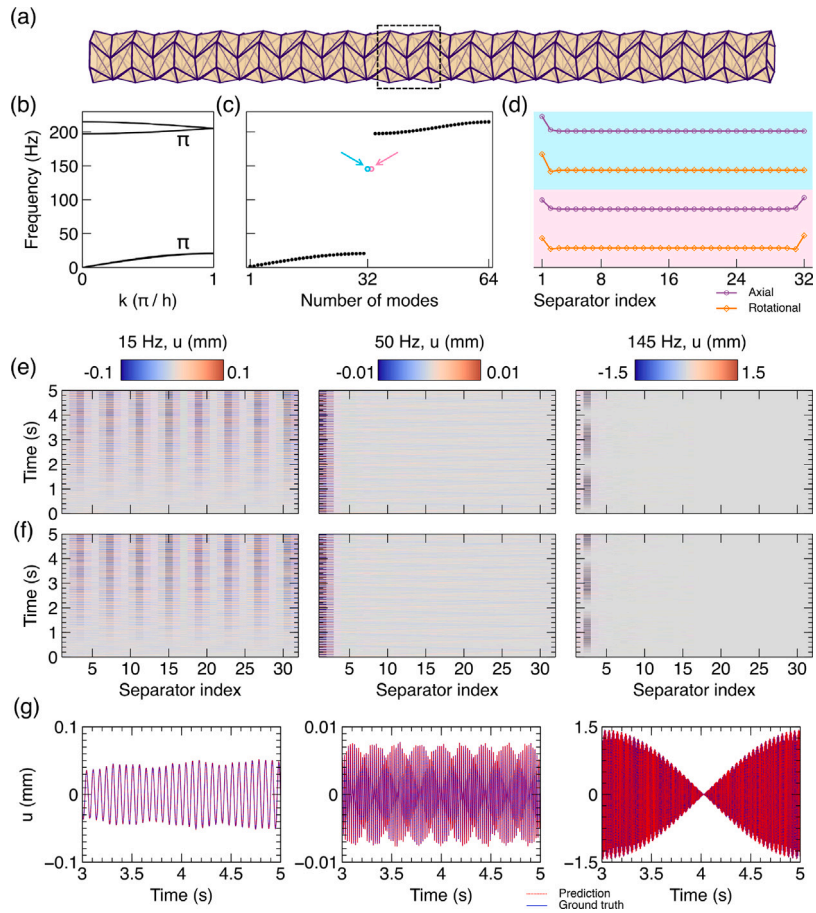

Fig. 2. Application of giDMD on the origami chain. (a) The schematic of the origami chain composed of Kresling origami with alternating chirality. The design parameters of origami are $h_0 = 30$ mm, $\theta_0 = \pm 70°$, $R = 36$ mm where h_0, θ_0, and R are the initial height, initial rotational angle, and radius of the cross-section, respectively. (b) The band structure calculated by the unit cell enclosed by black dashed line in (a). The Zak phases of the lower band and upper band are π. (c) The modes of the supercell formed by 16 unit cells. The black dots represent the bulk band. The cyan and pink dots represent the topological boundary states within the band gap. (d) The axial and rotational modes of the topological boundary states. (e) The simulated axial displacement along the origami chain at different frequencies in the pass band (15 Hz), stop band (50 Hz) and topological boundary states (145 Hz). (f) The corresponding predicted axial displacement using 60% training data (from 0 s to 3 s). (g) The comparison between ground truth (blue) and giDMD model (red) of the axial displacement of the second separator in the origami chain. The cases under 15 Hz, 50 Hz and 145 Hz are shown from left to right. (For interpretation of the references to color in this figure legend, the reader is referred to the web version of this article.)

bulk yet propagating along the boundary or surface. The topologically protected defect-immune wave propagation in the elastic topological metamaterials has been attracting significant attention [33–38]. Recently, the origami structures have been used as building blocks to construct topological metamaterials [14]. We adopt the existing design to construct the origami chain shown in Fig. 2(a). The unit cell enclosed by black dashed line contains two origamis with opposite chirality represented by initial rotational angle θ_0.

The band structure can be calculated by the linearized truss model (Appendix A) based on the small amplitude approximation after the application of periodic boundary condition (Bloch's theorem). As shown in Fig. 2(b), four bands appear in the first Brillouin zone. Two lower bands nearly overlap, and two upper bands are crossing to form a degeneracy point at the edge of the first Brillouin zone. To characterize the topology of this system, we calculate the topological invariant Zak phase for the 1D system. Because the bands are degenerate at the edge of the first Brillouin zone, the topological invariant Zak phase φ for qth and $(q+1)$-th bands is calculated through the Wilson-loop eigenvalues as indicated below:

$$\varphi_{q,q+1} = -\sum_{k=0}^{k-1} \mathrm{Im}\ln \begin{vmatrix} \langle U_k^q | U_k^q \rangle & \langle U_k^q | U_{k+1}^{q+1} \rangle \\ \langle U_k^{q+1} | U_{k+1}^q \rangle & \langle U_k^{q+1} | U_{k+1}^{q+1} \rangle \end{vmatrix} \tag{11}$$

where U_k^q denotes the mode at the Bloch wave vector k for the qth band [39]. This produces $\varphi_{1,2} = \varphi_{3,4} = \pi$ which are marked in Fig. 2(b). The nonzero topological invariant of the lower bands also ensures the topologically nontrivial band gap between the lower bands and the upper bands.

According to the bulk-edge correspondence, the topological boundary state will emerge within the band gap in the truncated origami chain. In Fig. 2(c), the eigenmodes of the truncated origami chain with 16 unit cells are calculated. As expected, two degenerate modes appear within the band gap. After checking the axial and rotational mode shapes of these two degenerate modes shown in Fig. 2(d), we confirm that these two degenerate modes are topological boundary states due to the concentrated displacement at the boundary.

Then, the wave propagation along the origami chain is calculated by the truss model (Appendix A) using the small-amplitude approximation (i.e., in the linear regime). The origami chain is excited by the harmonic motion of the first separator. The axial displacements of each separator over time are illustrated in Fig. 2(e) under different excitation frequencies, represented by the frequencies in pass band (15 Hz), stop band (50 Hz) and at the topological boundary state (145 Hz). At the frequency of 15 Hz, the vibration can affect the whole origami chain, while the vibration is localized at the boundary at the frequency of 50 Hz, as expected for such a band gap frequency. At the frequency of 145 Hz, where the topological boundary state emerges, the vibration is also localized at the boundary but with larger amplitude, representing the excitation of the corresponding eigenmode.

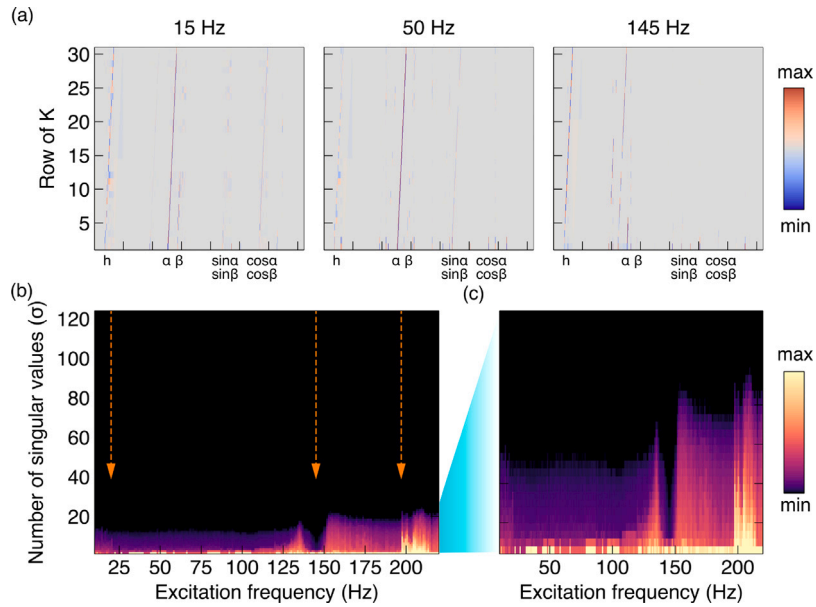

Fig. 3. Identification of topological boundary states in origami chain. (a) The rows of $\boldsymbol{K}$ matrix corresponding to the axial displacements of the origami chain at 15 Hz, 50 Hz and 145 Hz. The labels on the x axis show the corresponding control variables such as h, a, b, Ψ, α and β of every origami component in the origami chain. Only control variables corresponding to the nonzero and large entries in $\boldsymbol{K}$ are shown for better readability. The slanted lines indicate the nonzero values shift linearly with the increase of row of $\boldsymbol{K}$, representing the interaction between nearest origami elements. (b) The singular value spectrum of the $\boldsymbol{K}$ matrix under different excitation frequencies from 10 to 220 Hz. The orange dash arrows on two sides indicate the range of the bandgap, and one in the middle indicates the frequency of topological boundary states. (c) The zoom-in view by using 32 singular values.

The giDMD model for the origami chain is put forward using 60% training data (from 0 s to 3 s). The prediction and ground truth agree excellently, as evidenced by the same patterns in Figs. 2(e) and 2(f), and relative error smaller than 0.1% in general. Besides, Fig. 2(g) shows the detailed axial displacement of the second separator in the origami chain from simulation and giDMD. The overlapped curves exhibit the excellent agreement between ground truth and prediction. The highly accurate modeling of origami chain across frequencies confirms the ability of giDMD to model complex structures in the nearly linear regime of the corresponding dynamics.

We take the first 31 rows of the $\boldsymbol{K}$ matrix responsible for the calculation of the axial displacement of each separator in the origami chain. As shown in Fig. 3(a), the $\boldsymbol{K}$ matrix is fairly sparse with sparsity around 0.6 (the number of zero values in the matrix divided by the total number of elements in the matrix) for all three cases, where nonzero values are concentrated near the position indicating the information of height h, angles between crease lines and vertical direction α, β, and corresponding sine functions $\sin\alpha$, $\sin\beta$. It suggests that these geometrical variables are mainly important and responsible for the axial displacement of origami chain. Especially, at the frequency of the topological boundary state (145 Hz), the values for $\sin\alpha$, $\sin\beta$ are smaller than those of the other two frequencies, suggesting less importance of these two geometrical variables in forming topological boundary states. This may result from the strong localization of vibrations near the boundary, causing most geometrical variables to remain almost unchanged. Furthermore, the nonzero values shift linearly with the increase of the row of $\boldsymbol{K}$ slanted lines in Fig. 3(a), indicating that the displacement of each separator is related to geometrical variables of nearest origami elements. Note that the geometry information such as h marked in Fig. 3(a) generally indicates the geometrical variables of every origami component.

Similar to the DMD where the eigenvalue of the linear operator can characterize the system dynamics, we use the singular values of the $\boldsymbol{K}$ matrix to identify the 'state' of the system. The singular value spectra of the $\boldsymbol{K}$ matrix from 10 Hz to 220 Hz are shown in Fig. 3(b) to illustrate the difference. In the region of the pass band ($f \leq 20$ Hz, $f \geq 198$ Hz), the first several singular values are significantly larger than those in the region of stop band (20 Hz $\leq f \leq$ 198 Hz). At the frequency of topological boundary states, the singular values are particularly smaller than any of other frequencies as detailed in zoom-in view in Fig. 3(c). The smaller singular values at the frequency of topological boundary state may be induced by the absence of contribution from $\sin\alpha$, $\sin\beta$ compared with other frequencies. We also notice that there are smaller singular values around 145 Hz but the smallest one is at 145 Hz. The singular values are large outside 145 Hz and the ones within the band gap region (20 Hz $\leq f \leq$ 198 Hz) are used to describe the localized states near the boundary due to the band gap. This can be a data-driven way to identify the frequency of topological boundary states.

3.2. Dynamic motion in the dual origami structure

The next example is the dual origami structure exhibiting rich dynamic motions under excitation. This structure is composed of two bistable origami elements with opposite chirality as shown in Fig. 4(a), in which u_0 and ϕ_0 are the input axial and rotational excitations at the first separator, and u_1, ϕ_1 and u_2, ϕ_2 are the axial and rotational displacements at the second and third separators, respectively. In the previously reported experimental study [16], under the excitation in different frequencies, the structure will feature periodic motion (5–9 Hz, 14–16 Hz, 18 Hz, 23–24 Hz) and chaotic motion (10–13 Hz, 17 Hz, 19–22 Hz). Note that due to combination of two bistable origamis, the periodic motion can be further identified as intrawell periodic motion (5–9 Hz, 18 Hz, 23–24 Hz), and interwell periodic motion (14–16 Hz). The intra- and inter- well behaviors are further elaborated in the Ref. [16]. The experimental setup is shown in Fig. 4(b) and detailed in Appendix A. Although this structure is simpler than the previous example, it is under the large-amplitude excitation region and hence displays the corresponding hallmarks of nonlinear dynamics, including the above mentioned chaotic motion.

To demonstrate our method, we choose two typical cases where periodic motion and chaotic motion are represented by 5 Hz and 17 Hz, respectively. After obtaining the $\boldsymbol{K}$ matrix from the sparse regression, where the sparsity of $\boldsymbol{K}$ matrix is around 0.7, we check the first row of the $\boldsymbol{K}$ matrix responsible for the calculation of axial displacement u_1.

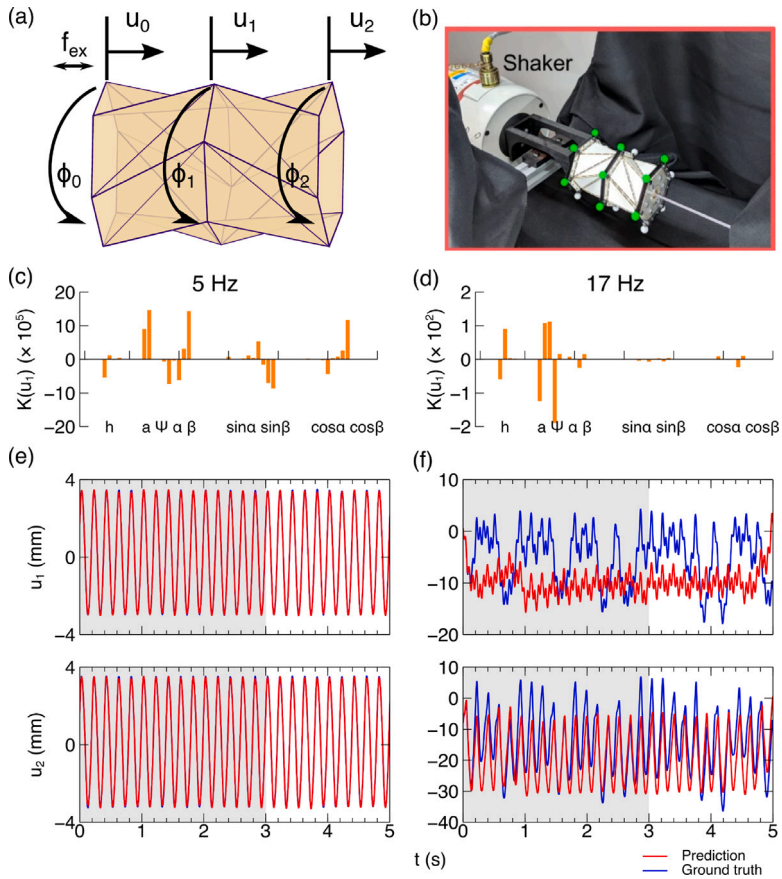

Fig. 4. Application of giDMD on the dual origami structure. (a) The schematic of the dual origami structure with opposite chirality. (b) The image of experimental setup for the vibration test from the Ref. [16]. Copyright 2020 Springer Nature. The design parameters of origami are $h_0 = 50$ mm, $\theta_0 = \pm 70°$, $R = 36$ mm where h_0, θ_0, and R are the initial height, initial rotational angle, and radius of the cross-section, respectively. The input excitation is applied by a shaker, and the motions are captured by two action cameras and quantified by the digital image correlation program. (c)(d) The row of $\boldsymbol{K}$ matrix corresponding to the axial displacement u_1 at the frequency of 5 Hz and 17 Hz, respectively. The labels on the x axis show the corresponding control variables such as h, a, b, Ψ, α and β of two origami components. Only control variables corresponding to the nonzero and large entries in $\boldsymbol{K}$ are shown due to the better readability. (e) The prediction of axial displacement u_1 and u_2 using giDMD at the frequency of 5 Hz. (f) The prediction of axial displacement u_1 and u_2 using giDMD at the frequency of 17 Hz. The gray shaded areas represent the training data. The ground truth is shown in blue and the prediction is shown in red. (For interpretation of the references to color in this figure legend, the reader is referred to the web version of this article.)

The case for 5 Hz is shown in Fig. 4(c). The first row of the $\boldsymbol{K}$ matrix is sparse so that nonzero values only appear in several positions standing for the information of h, a, Ψ, α, β, sine and cosine functions of α and β, suggesting that these geometrical variables are responsible for the axial motion of the second separator. In comparison, at the frequency of 17 Hz, nonzero values emerge in similar positions but with much smaller values in Fig. 4(d). Besides, the sine and cosine functions of α and β are contributing less to the axial motion of the second separator due to the smaller values than other geometrical variables. Compared with the origami chain where the length of crease lines and the folding angle do not significantly contribute to the axial displacement, in the present case, the length of crease lines and folding angle are major contributions to the axial displacement for the dual origami structure. The possible reason can be the smaller amplitude excitation (i.e., linear regime) of the origami chain, leading to the representation of a, b and Ψ by the function of h. After sparse regression, the contributions of a, b and Ψ can be approximated by h, whereas large-amplitude excitation (nonlinear regime) in dual origami structure results in the failure to represent a, b and Ψ using h. Similar to the analysis of the $\boldsymbol{K}$ matrix in Section 3.1, the geometry information marked in Fig. 4(c) generally indicates the geometrical variables of two origami components.

We then predict the axial displacements u_1 and u_2 at the frequency of 5 Hz and 17 Hz. As shown in Fig. 4(e), the prediction and ground truth agree excellently with 60% training data, as evidenced by the overlap of red curves and blue curves. In stark contrast, the predictions at the frequency of 17 Hz do not match with the ground truth in a precise manner (Fig. 4(f)). Although the sudden change in the chaotic motion cannot be predicted, the predicted results still show clear differences from the periodic motion (Fig. 4(e)), i.e., they carry the blueprint of the observed chaotic dynamics. Therein, u_1 is more chaotic than u_2 and thus the prediction is better in u_2. Note that the prediction results of intrawell periodic motion at other frequencies are similar to Fig. 4(e), while the ones of chaotic motion at other frequencies are similar to Fig. 4(f).

The spectral analysis is conducted to show the frequency response under the excitation in different frequencies. In Fig. 5(a), the spectra for u_1 and u_2 in different frequencies are obtained by the fast Fourier transform of the experimental data after normalization. It is obvious that along the diagonal direction of each panel, there are responses at the same frequency as the excitation frequency. Apart from that, the periodic motion and the chaotic motion can be clearly identified from the increase of lower frequency components. The 'state' of the structure is also marked in Figs. 5(a) and (b), where green, orange and purple shaded areas indicate the intrawell periodic motion, interwell periodic motion and chaotic motion. Fig. 5(b) illustrates the spectra for u_1 and u_2 based on the prediction results. It can be seen that the spectra in the region of intrawell periodic motion (5–9 Hz, 18 Hz, 23–24 Hz) agree with the ground truth excellently. However, giDMD fails to predict the interwell periodic motion (14–16 Hz), where the predictions blow up to infinity at some time point, resulting in the failure of spectral analysis. The interwell periodic motion describes the scenario where

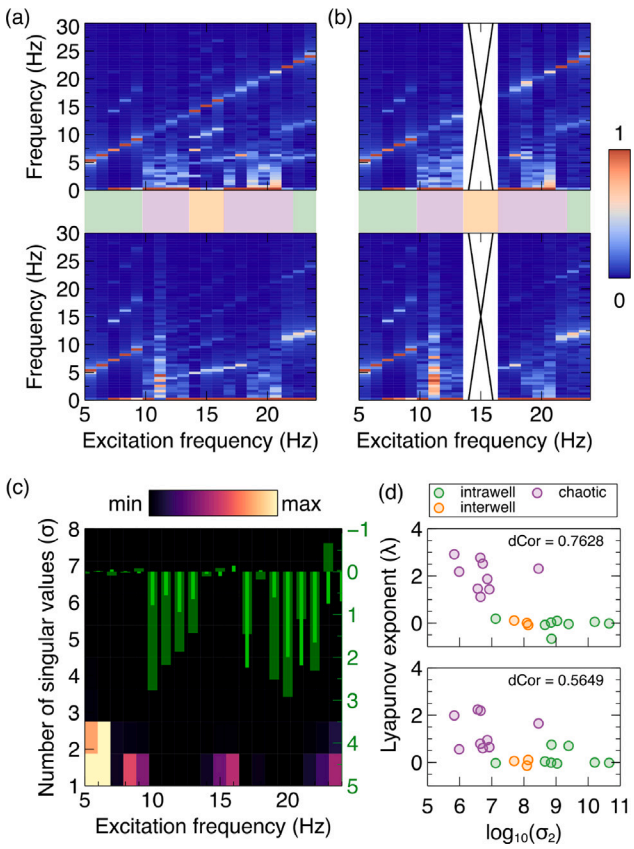

Fig. 5. Identification of intrawell periodic, interwell periodic and chaotic motion. (a) The spectrum analysis of the experimental axial displacements u_1 (the first panel) and u_2 (the second panel) under different excitation frequencies from 5 to 24 Hz. (b) The corresponding spectral analysis based on the predicted axial displacements u_1 (the first panel) and u_2 (the second panel). The white area with a cross represents the failure of the prediction. The green, orange and purple shaded areas represent the frequencies of intrawell periodic motion, interwell periodic motion and chaotic motion. (c) The singular value spectrum of the $\boldsymbol{K}$ matrix under different excitation frequencies from 5 to 24 Hz. The Lyapunov exponents of u_1 and u_2 under different excitation frequencies are also shown in dark green and bright green, respectively. (d) The relation between the second singular values σ_2 and the Lyapunov exponents λ under different excitation frequencies. The intrawell periodic motion, interwell periodic motion and chaotic motion are represented in green, orange and purple circles. The distance correlation between logarithm-scale second singular values and Lyapunov exponents are shown in both graphs. (For interpretation of the references to color in this figure legend, the reader is referred to the web version of this article.)

u_1 and u_2 feature a large difference, as well as ϕ_1 and ϕ_2, i.e., in the regime of significant axial and rotational differences across origami separators. In such case, the blow-up phenomena in the prediction are due to the unstable dynamical system produced by the giDMD model. Understanding how to extend the giDMD approach to capture such a scenario remains an interesting open question for further investigation. In the region of chaotic motion (10–13 Hz, 17 Hz, 19–22 Hz), the spectra from the predicted results show qualitative agreement with the ground truth featured by the increased magnitude in the low frequency range, despite the failure to capture the intermittent variation in chaotic motion as shown in Fig. 4(f). These findings imply that giDMD can predict the chaotic motion to some extent.

Similar to Section 3.1, we study the feasibility of using the $\boldsymbol{K}$ matrix to identify the 'state' of the dual origami structure. Fig. 5(c) shows the singular values σ of the $\boldsymbol{K}$ matrix at different frequencies, where different singular value spectra appear in different frequencies. We notice that in the frequency range corresponding to the chaotic motion, the singular values are particularly smaller than others. To characterize the origami dynamics, the Lyapunov exponents for u_1 and u_2 are shown by bright green and dark green in Fig. 5(c), calculated by the Rosenstein's method [40]. As is well-known, the larger Lyapunov exponent suggests more chaotic dynamics. From our results, we can deduce that smaller singular values correspond to larger Lyapunov exponent. In Fig. 5(d), we choose the second singular value of each $\boldsymbol{K}$ matrix σ_2 to compare with Lyapunov exponents for u_1 (top panel) and u_2 (bottom panel). It is noticed that there are clear boundaries among chaotic motion (smallest values), interwell periodic motion and intrawell periodic motion (largest values). Besides, there is the fairly strong relation characterized by the distance correlation (quotient of the distance covariance and the product of the distance standard deviations) between logarithm-scaled second singular values and Lyapunov exponents, resulting in $dCor = 0.7628$ and $dCor = 0.5649$ for u_1 and u_2. The correlation between the singular values and the Lyapunov exponents of the dynamics system has not only emerged in our data-driven study, but also in several theoretical studies aimed at calculating Lyapunov exponent [41,42]. Therefore, based on the above results, one can identify the intrawell, or interwell periodic motion or the chaotic motion of the dual origami structure.

4. Discussion and conclusion

The $\boldsymbol{K}$ matrix serves as the control matrix in the giDMD, which will convert the control $\boldsymbol{Y}$ to $\boldsymbol{S}$, expressed by $\boldsymbol{S} = \boldsymbol{X} - \boldsymbol{X}'$. Since the state $\boldsymbol{X}$ corresponds to the displacement and velocity of each separator at each time step, $\boldsymbol{S}$ contains the information of velocity and acceleration. Essentially, $\boldsymbol{K}$ is found to describe the velocity and acceleration using geometrical parameters in origami structures. The sparsity of $\boldsymbol{K}$ matrix shows that the velocity and acceleration of the origami structure are only related to a few geometrical parameters. This can also be implied by the governing equation of motion of origami as shown in the Appendix A and derived equations. These governing equations of motion of origami contain the combination of geometrical parameters explicitly or implicitly. The $\boldsymbol{K}$ matrix essentially selects the important geometrical parameters listed in the $\boldsymbol{Y}$ matrix by the values of its entries. Indeed, this is done through the original system dynamics (and this data-driven approach), rather than by the more traditional method of inducing parametric variations and observing the relevant response. This is the reason why giDMD works well in origami dynamics and is only related to the several geometrical variables, resulting in the sparse $\boldsymbol{K}$ matrix. In a sense, one can argue that the material in Appendix A represents the traditional modeling approach (based on constitutive laws) towards the origami system of interest, while the giDMD represents a modern, data-driven variant thereof. Even when the governing equation is not available, this approach can still be used to potentially model the origami dynamics from experimental data. Furthermore, our method can also be interpreted by the mode superposition, since the individual entries k_{ij} of $\boldsymbol{K}$ matrix can be expressed as $k_{ij} = \boldsymbol{u}_j^T \boldsymbol{\Sigma}^{-1} \boldsymbol{V}^T \boldsymbol{s}_i$ after the singular value decomposition, $\boldsymbol{Y} = \boldsymbol{U}\boldsymbol{\Sigma}\boldsymbol{V}^T$, where $\boldsymbol{u}_j^T$ is the jth row of $\boldsymbol{U}$ and $\boldsymbol{s}_i^T$ is the ith row of $\boldsymbol{S}$. This results in different $\boldsymbol{K}$ matrix in the same origami structure under different frequencies. For the consistency of the narrative, we fix the training ratio to be 60% in the main text, but we also show the giDMD modeling in other training ratios in Appendices B and C including error analysis and identification of states of origami structures. Our approach demonstrates the efficacy in different training ratios and the ability to identify origami dynamics.

In this work, we propose the method of giDMD to learn the origami dynamics that gives rise to origami coupled motions from pure observation data (experiment data and simulation data). We show the better performance of giDMD characterized by the prediction accuracy compared with DMDc. In the two example origami structures we apply our method on, giDMD can not only predict the origami behaviors under different frequencies, but also highlight an ability to identify the 'state' of origami structures. Furthermore, giDMD offers insights

into the importance of geometries in the governing motion law of origami. giDMD has better performance in the linear (or nearly linear) region of origami dynamics, while there are still some challenges in describing chaotic dynamics within the nonlinear regime. In the latter, giDMD starts to fail in connection to the goal of accurate prediction, but it can still help with the identification of the origami state. The giDMD provides a substantial capability to model origami dynamics in an efficient (fast computation) and interpretable way. Although we primarily demonstrate our method on two specific structures, future work can be devoted into more complex origami structures across scales and not limited to the Kresling origami. Besides, whether the origami systems driven by the non-periodic excitation can be modeled by our giDMD method is worthwhile to explore. Indeed, the further extension of giDMD to other such geometrically nonlinear systems is a topic currently under active investigation and relevant results will be reported in due course.

Declaration of competing interest

The authors declare that they have no known competing financial interests or personal relationships that could have appeared to influence the work reported in this paper.

Data availability

Data will be made available on request.

Acknowledgments

We are grateful for the support from the U.S. National Science Foundation: S.L., Y.M., K.Y. and J.Y. (Grant No. 1933729 and 2201612), P.G.K. (Grant No. DMS 2204702). J.Y. acknowledges the support from SNU-IAMD, SNU-IOER, and National Research Foundation, South Korea grants funded by the Korea government [2023R1A2C2003705 and 2022H1D3A2A03096579 (Brain Pool Plus by the Ministry of Science and ICT)]. K.Y. is supported by Funai Foundation for Information Technology.

Appendix A. Data acquisition

A.1. Experimental data

In the example of the dual origami structure, the raw experimental data was used for the giDMD model. The experimental data and experimental procedures were detailed in the Ref. [16]. The dynamic test was conducted on a dual triangulated cylindrical origami structure. The design parameters of origami were $h_0 = 50$ mm, $\theta_0 = \pm 70°$, $R = 36$ mm which are the initial height, initial rotational angle, and radius of the cross-section, respectively. The left origami is in negative chirality ($\theta_0 = -70°$) and the right origami is in positive chirality ($\theta_0 = +70°$). The left end of the dual origami structure was connected to the shaker (LDS V406 M4-CE, Brüel & Kjær) which applied the single-frequency harmonic excitation to the system. The motion of spherical markers attached to the separators was captured by two action cameras in 240 frames per second and quantified by digital image correlation. The triangulation method was used to find the three-dimensional coordinates of the spherical markers, resulting in the axial displacement u and rotational displacement ϕ of each separator.

Table A.1
Design parameters for single origami and origami chain.

m (kg)	j (kg m^2)	N	h_0 (m)	R (m)	θ_0 (°)
58.8×10^{-3}	6.77×10^{-5}	6	30×10^{-3}	36×10^{-3}	±70

Table A.2
Mechanical parameters for single origami and origami chain.

k_a (N m^{-1})	k_b (N m^{-1})	k_ψ (N m rad^{-1})
6055	3743	7.277×10^{-3}

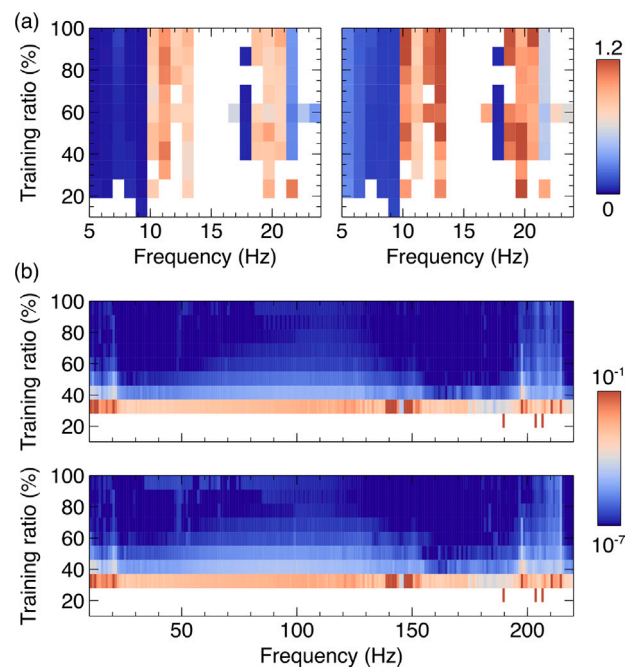

Fig. B.6. The prediction accuracy for the dual origami structure and the origami chain using different training ratios. (a) The relative errors as a function of training ratio of axial and rotational displacement in different frequencies for dual origami structure are shown in the left and right panel, respectively. (b) The relative errors as a function of training ratio of axial and rotational displacement in different frequencies for the origami chain are shown in the left and right panel, respectively. The white regions indicate the failure of the prediction in (a) and (b).

A.2. Simulation data

In the example of single origami and origami chain, the simulation data was used for the giDMD model. The design parameters and mechanical parameters used in the numerical simulation are shown in Tables A.1 and A.2, respectively.

The mechanical parameters k_a, k_b represent the axial spring constant along the crease a, b, and k_ψ represents the torsional spring constant along the bottom crease.

The simulations of the single origami and origami chain under excitation in different frequencies are conducted based on the truss model regarding Kresling unit cell as inter-polygonal spring connecting separators with mass m and rotational inertia j [6,13,14]. The equation of motion of the separator can be expressed as:

$$m_n \ddot{u}_n + F_n(\delta u_n, \delta\phi_n) - F_{n-1}(\delta u_{n-1}, \delta\phi_{n-1}) = 0 \tag{A.1a}$$

$$j_n \ddot{\phi}_n + T_n(\delta u_n, \delta\phi_n) - T_{n-1}(\delta u_{n-1}, \delta\phi_{n-1}) = 0 \tag{A.1b}$$

where $\delta u_n = u_n - u_{n+1}$ and $\delta\phi_n = \phi_n - \phi_{n+1}$. The subscript n denotes the nth separator. The force and torque in Eq. (A.1a) and Eq. (A.1b) can be further expanded by the summation of the contribution from each

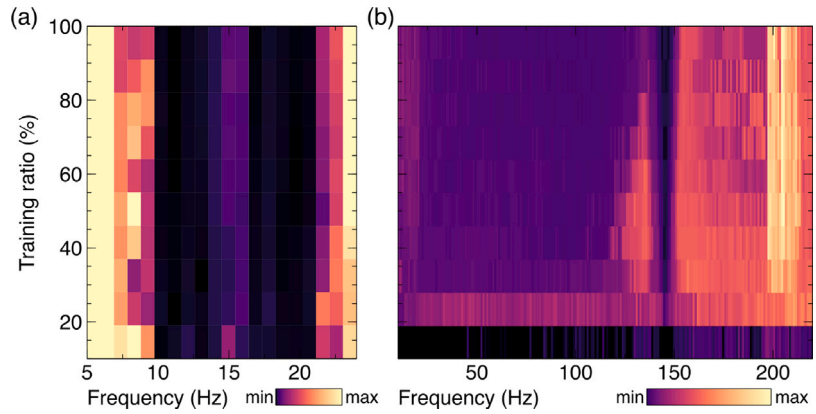

Fig. C.7. The singular values of $\boldsymbol{K}$ matrix for dual origami structure and origami chain using different training ratios. (a) The first singular value of $\boldsymbol{K}$ matrix as a function of training ratio in different frequencies for dual origami structure. (b) The fifth singular value of $\boldsymbol{K}$ matrix as a function of training ratio in different frequencies for origami chain.

spring as below:

$$\begin{aligned} F_n(\delta u_n, \delta\phi_n) = {} & k_{an} N(\delta u_n - h_0)(1 - \frac{a_0}{a_n}) \\ & + k_{bn} N(\delta u_n - h_0)(1 - \frac{b_0}{b_n}) \\ & + 2k_{\Psi n} N R h_0(\Psi_0 - \Psi_n) \\ & \times \frac{\cos\frac{\pi}{N} - \cos(\delta\phi_n + \theta_0)}{R^2[\cos\frac{\pi}{N} - \cos(\delta\phi_n + \theta_0)]^2 + (h_0 - \delta u_n)^2} \end{aligned} \tag{A.2a}$$

$$\begin{aligned} T_n(\delta u_n, \delta\phi_n) = {} & k_{an} N R^2 \sin(\delta\phi_n + \theta_0 - \frac{\pi}{N})(1 - \frac{a_0}{a_n}) \\ & + k_{bn} N R^2 \sin(\delta\phi_n + \theta_0 + \frac{\pi}{N})(1 - \frac{b_0}{b_n}) \\ & + 2k_{\Psi n} N R h_0(\Psi_0 - \Psi_n) \\ & \times \frac{\sin(\delta\phi_n + \theta_0)(h_0 - \delta u_n)}{R^2[\cos\frac{\pi}{N} - \cos(\delta\phi_n + \theta_0)]^2 + (h_0 - \delta u_n)^2} \end{aligned} \tag{A.2b}$$

where the parameters with subscript 0 denote the initial origami configuration.

The calculation of the band structure is based on the linearized truss model of the unit cell in order to represent the small amplitude excitation. The unit cell contains two origami elements whose front separators denote the sites (1) and (2). The linearized equations of motion can be expressed as:

$$\begin{aligned} & m_n \ddot{u}_n^{(1)} - \alpha_{11}(u_n^{(2)} - u_n^{(1)}) - \beta_{11}(u_{n-1}^{(2)} - u_n^{(1)}) \\ & - \alpha_{12}(\phi_n^{(2)} - \phi_n^{(1)}) - \beta_{12}(\phi_{n-1}^{(2)} - \phi_n^{(1)}) = 0 \end{aligned} \tag{A.3a}$$

$$\begin{aligned} & m_n \ddot{u}_n^{(2)} - \alpha_{11}(u_n^{(1)} - u_n^{(2)}) - \beta_{11}(u_{n+1}^{(1)} - u_n^{(2)}) \\ & - \alpha_{12}(\phi_n^{(1)} - \phi_n^{(2)}) - \beta_{12}(\phi_{n+1}^{(1)} - \phi_n^{(2)}) = 0 \end{aligned} \tag{A.3b}$$

$$\begin{aligned} & j_n \ddot{\phi}_n^{(1)} - \alpha_{21}(u_n^{(2)} - u_n^{(1)}) - \beta_{21}(u_{n-1}^{(2)} - u_n^{(1)}) \\ & - \alpha_{22}(\phi_n^{(2)} - \phi_n^{(1)}) - \beta_{22}(\phi_{n-1}^{(2)} - \phi_n^{(1)}) = 0 \end{aligned} \tag{A.3c}$$

$$\begin{aligned} & j_n \ddot{\phi}_n^{(2)} - \alpha_{21}(u_n^{(1)} - u_n^{(2)}) - \beta_{21}(u_{n+1}^{(1)} - u_n^{(2)}) \\ & - \alpha_{22}(\phi_n^{(1)} - \phi_n^{(2)}) - \beta_{22}(\phi_{n+1}^{(1)} - \phi_n^{(2)}) = 0 \end{aligned} \tag{A.3d}$$

where the coefficients can be derived from the second derivative of the potential energy of each unit cell as detailed in the Ref. [14]. With the design parameters and mechanical parameters in Tables A.1 and A.2, the coefficients can be determined to be $\alpha_{11} = \beta_{11} = 26850$ N m^{-1}, $\alpha_{12} = -\beta_{12} = -819.8$ N rad^{-1} and $\alpha_{22} = \beta_{22} = 26.07$ N m rad^{-1}. The periodic boundary condition (Bloch's theorem) is then applied to the linearized equation of motion, such that $u_{n-1}^{(2)} = u_n^{(2)} e^{-2ikh_0}$, $\phi_{n-1}^{(2)} = \phi_n^{(2)} e^{-2ikh_0}$, $u_{n+1}^{(1)} = u_n^{(1)} e^{2ikh_0}$ and $\phi_{n+1}^{(1)} = \phi_n^{(1)} e^{2ikh_0}$. The band structure $\omega(k)$ can be obtained by solving the eigenvalue equation as a function of the Bloch wave vector k in the first Brillouin zone:

$$[\omega^2 + \hat{D}(k)]U = 0 \tag{A.4}$$

Here, ω denotes the angular frequency. $\hat{D}(k)$ is the dynamical matrix as a function of k, and U is the corresponding eigenmode expressed as $U = [\sqrt{m}u^{(1)}, \sqrt{m}u^{(2)}, \sqrt{j}\phi^{(1)}, \sqrt{j}\phi^{(2)}]^T$.

Appendix B. Error analysis in different training ratios

Although the training ratio for the giDMD model of our aforementioned examples is set to be 60%, we also investigate the sufficiency of the training ratio to build an effective and reliable model to describe the origami dynamics. The relative error in different training ratios is calculated for two examples (Fig. B.6(a) for the dual origami structure and Fig. B.6(b) for the origami chain). Fig. B.6(a) shows the relative error of axial and rotational displacement in the left and right panels, respectively. It can be seen that 20% training ratio is enough to build the effective giDMD model for most cases of intrawell periodic motion in the dual origami structure. However, giDMD fails to model the interwell periodic motion no matter what the training ratio is. The effective modeling for the chaotic motion can be achieved as early as when the training ratio is 20%. The corresponding model cannot precisely describe the intermittent change of chaotic motion as illustrated in Fig. 4(f) in the main text, resulting in the large relative error. However, it can show the spectral features of the chaotic motion (large low-frequency components) as shown in Fig. 5(b). Note that large training ratio does not always guarantee the effective giDMD model as shown by the white areas in the region of large training ratios.

Fig. B.6(b) shows the relative error of axial and rotational displacement in the top and bottom panels, respectively. It can be seen that the effective model can be constructed as early as when the training ratio is 30%. Besides, the model across frequencies can be built with high accuracy. The error analysis in different training ratios shows the efficacy of our approach with fewer training data, which demonstrates the possibility of early prediction in origami dynamics.

Appendix C. Identification of state in different training ratios

As stated in the main text, the 'state' of the origami structure may be induced by the singular value of $\boldsymbol{K}$ matrix. We further calculate the singular values of $\boldsymbol{K}$ matrix in different training ratios to identify the 'state' in origami structures. The second singular value of $\boldsymbol{K}$ matrix in different training ratios is calculated for the dual origami structure (Fig. C.7(a)), and the fifth singular value is calculated for the origami chain (Fig. C.7(b)). Fig. C.7(a) reveals that the intrawell periodic motion, interwell periodic motion and chaotic motion can be

initially identified by distinct values when the training ratio is only 10%, although it should be noticed that at this training ratio the giDMD models for different frequencies are not adequate to describe the origami dynamics. In the origami chain, the fifth singular value is used to conduct identification to have a stronger contrast although other singular values also work. The topological boundary state can be identified when the training ratio is 20% even though the model is not effectively built. This study on different training ratios indicates that our approach of giDMD can identify the 'state' of origami structures at the early stage, which helps with the early diagnosis and identification of the origami structure.

References

[1] E.T. Filipov, T. Tachi, G.H. Paulino, Origami tubes assembled into stiff, yet reconfigurable structures and metamaterials, Proc. Natl. Acad. Sci. 112 (40) (2015) 12321–12326.

[2] C. Lv, D. Krishnaraju, G. Konjevod, H. Yu, H. Jiang, Origami based mechanical metamaterials, Sci. Rep. 4 (1) (2014) 1–6.

[3] H. Yasuda, J. Yang, Reentrant origami-based metamaterials with negative Poisson's ratio and bistability, Phys. Rev. Lett. 114 (18) (2015) 185502.

[4] C. Jianguo, D. Xiaowei, Z. Ya, F. Jian, T. Yongming, Bistable behavior of the cylindrical origami structure with Kresling pattern, J. Mech. Des. 137 (6) (2015) 061406.

[5] B.H. Hanna, J.M. Lund, R.J. Lang, S.P. Magleby, L.L. Howell, Waterbomb base: A symmetric single-vertex bistable origami mechanism, Smart Mater. Struct. 23 (9) (2014) 094009.

[6] H. Yasuda, T. Tachi, M. Lee, J. Yang, Origami-based tunable truss structures for non-volatile mechanical memory operation, Nat. Commun. 8 (1) (2017) 1–7.

[7] S. Miyashita, S. Guitron, M. Ludersdorfer, C.R. Sung, D. Rus, An untethered miniature origami robot that self-folds, walks, swims, and degrades, in: 2015 IEEE International Conference on Robotics and Automation, ICRA, IEEE, 2015, pp. 1490–1496.

[8] S.A. Zirbel, R.J. Lang, M.W. Thomson, D.A. Sigel, P.E. Walkemeyer, B.P. Trease, S.P. Magleby, L.L. Howell, Accommodating thickness in origami-based deployable arrays, J. Mech. Des. 135 (11) (2013).

[9] B.J. Edmondson, L.A. Bowen, C.L. Grames, S.P. Magleby, L.L. Howell, T.C. Bateman, Oriceps: Origami-inspired forceps, in: Smart Materials, Adaptive Structures and Intelligent Systems, Vol. 56031, American Society of Mechanical Engineers, 2013, V001T01A027.

[10] T.G. Nelson, R.J. Lang, S.P. Magleby, L.L. Howell, Curved-folding-inspired deployable compliant rolling-contact element (D-CORE), Mech. Mach. Theory 96 (2016) 225–238.

[11] X. Deng, J. Zhao, J. Cai, X. Liu, Tunable origami metamaterial with arbitrary single-curvature configuration, Mech. Mach. Theory 171 (2022) 104745.

[12] S. Lyu, B. Qin, H. Deng, X. Ding, Origami-based cellular mechanical metamaterials with tunable Poisson's ratio: Construction and analysis, Int. J. Mech. Sci. 212 (2021) 106791.

[13] H. Yasuda, Y. Miyazawa, E.G. Charalampidis, C. Chong, P.G. Kevrekidis, J. Yang, Origami-based impact mitigation via rarefaction solitary wave creation, Sci. Adv. 5 (5) (2019) eaau2835.

[14] Y. Miyazawa, C.-W. Chen, R. Chaunsali, T.S. Gormley, G. Yin, G. Theocharis, J. Yang, Topological state transfer in Kresling origami, Commun. Mater. 3 (1) (2022) 1–10.

[15] C. Huang, T. Tan, Z. Wang, S. Zhang, F. Yang, Z. Lin, Z. Yan, Origami dynamics based soft piezoelectric energy harvester for machine learning assisted self-powered gait biometric identification, Energy Convers. Manage. 263 (2022) 115720.

[16] H. Yasuda, K. Yamaguchi, Y. Miyazawa, R. Wiebe, J.R. Raney, J. Yang, Data-driven prediction and analysis of chaotic origami dynamics, Commun. Phys. 3 (1) (2020) 1–8.

[17] C. Zhou, B. Wang, J. Ma, Z. You, Dynamic axial crushing of origami crash boxes, Int. J. Mech. Sci. 118 (2016) 1–12.

[18] K. Champion, B. Lusch, J.N. Kutz, S.L. Brunton, Data-driven discovery of coordinates and governing equations, Proc. Natl. Acad. Sci. 116 (45) (2019) 22445–22451.

[19] R. Iten, T. Metger, H. Wilming, L. Del Rio, R. Renner, Discovering physical concepts with neural networks, Phys. Rev. Lett. 124 (1) (2020) 010508.

[20] M. Raissi, P. Perdikaris, G.E. Karniadakis, Physics-informed neural networks: A deep learning framework for solving forward and inverse problems involving nonlinear partial differential equations, J. Comput. Phys. 378 (2019) 686–707.

[21] S.L. Brunton, J.L. Proctor, J.N. Kutz, Discovering governing equations from data by sparse identification of nonlinear dynamical systems, Proc. Natl. Acad. Sci. 113 (15) (2016) 3932–3937.

[22] J.H. Tu, C.W. Rowley, D.M. Luchtenburg, S.L. Brunton, J.N. Kutz, On dynamic mode decomposition: Theory and applications, J. Comput. Dynam. 1 (2) (2014) 391.

[23] J.N. Kutz, S.L. Brunton, B.W. Brunton, J.L. Proctor, Dynamic Mode Decomposition: Data-Driven Modeling of Complex Systems, SIAM, 2016.

[24] P.J. Schmid, Dynamic mode decomposition of numerical and experimental data, J. Fluid Mech. 656 (2010) 5–28.

[25] S. Li, L.M. Roger, J. Klein-Seetharaman, L.J. Cowen, N.A. Lewinski, J. Yang, Data-driven discovery of spatiotemporal coherent patterns in pulsating soft coral tentacle motion with dynamic mode decomposition, Phys. Rev. Res. 5 (2023) 013175.

[26] H.N. Ingabire, K. Wu, J.T. Amos, S. He, X. Peng, W. Wang, M. Li, J. Chen, Y. Feng, N. Rao, et al., Analysis of ECG signals by dynamic mode decomposition, IEEE J. Biomed. Health Inf. 26 (5) (2021) 2124–2135.

[27] A. Saito, T. Kuno, Data-driven experimental modal analysis by dynamic mode decomposition, J. Sound Vib. 481 (2020) 115434.

[28] S. Li, P.G. Kevrekidis, J. Yang, Characterization of elastic topological states using dynamic mode decomposition, Phys. Rev. B 107 (2023) 184308.

[29] J.L. Proctor, S.L. Brunton, J.N. Kutz, Dynamic mode decomposition with control, SIAM J. Appl. Dyn. Syst. 15 (1) (2016) 142–161.

[30] E. Hansen, S.L. Brunton, Z. Song, Swarm modelling with dynamic mode decomposition, IEEE Access (2022).

[31] E. Kaiser, J.N. Kutz, S.L. Brunton, Sparse identification of nonlinear dynamics for model predictive control in the low-data limit, Proc. R. Soc. Lond. Ser. A Math. Phys. Eng. Sci. 474 (2219) (2018) 20180335.

[32] L. Zhang, H. Schaeffer, On the convergence of the SINDy algorithm, Multiscale Model. Simul. 17 (3) (2019) 948–972.

[33] G. Ma, M. Xiao, C.T. Chan, Topological phases in acoustic and mechanical systems, Nat. Rev. Phys. 1 (4) (2019) 281–294.

[34] S. Li, I. Kim, S. Iwamoto, J. Zang, J. Yang, Valley anisotropy in elastic metamaterials, Phys. Rev. B 100 (19) (2019) 195102.

[35] T.-W. Liu, F. Semperlotti, Tunable acoustic valley–hall edge states in reconfigurable phononic elastic waveguides, Phys. Rev. A 9 (1) (2018) 014001.

[36] S. Li, J. Yang, Topological transition in spiral elastic valley metamaterials, Phys. Rev. A 15 (1) (2021) 014058.

[37] J. Vila, R.K. Pal, M. Ruzzene, Observation of topological valley modes in an elastic hexagonal lattice, Phys. Rev. B 96 (13) (2017) 134307.

[38] S. Li, D. Zhao, H. Niu, X. Zhu, J. Zang, Observation of elastic topological states in soft materials, Nat. Commun. 9 (1) (2018) 1–9.

[39] H.-X. Wang, G.-Y. Guo, J.-H. Jiang, Band topology in classical waves: Wilson-loop approach to topological numbers and fragile topology, New J. Phys. 21 (9) (2019) 093029.

[40] M.T. Rosenstein, J.J. Collins, C.J. De Luca, A practical method for calculating largest Lyapunov exponents from small data sets, Physica D 65 (1–2) (1993) 117–134.

[41] K. Geist, U. Parlitz, W. Lauterborn, Comparison of different methods for computing Lyapunov exponents, Progress of theoretical physics 83 (5) (1990) 875–893.

[42] L. Barreira, C. Valls, Lyapunov regularity via singular values, Trans. Amer. Math. Soc. 369 (12) (2017) 8409–8436.